Heliyon 10 (2024) e36489

Contents lists available at ScienceDirect

Heliyon

journal homepage: www.cell.com/heliyon

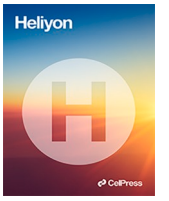

Research article

Determining the characteristics of representative volume elements in severely deformed aluminum-matrix composite

Amir Hossein Assari [a,*], Negar Shaghaghi [b], Saeid Yaghoobi [c], Sahar Ghaderi [d]

[a] Department of Materials Science and Engineering, Sahand University of Technology, Tabriz, Iran
[b] School of Chemical Engineering, College of Engineering, University of Tehran, 16th Azar St., Enghelab Sq., Tehran, Iran
[c] Department of Mechanical Engineering, Bu-Ali Sina University, Hamedan, Iran
[d] Mechanical Engineering Department, Hamedan University of Technology, Hamedan, Iran

ARTICLE INFO

Keywords:
Finite element analysis
Metal-matrix composites
Mechanical properties
Elasticity

ABSTRACT

The accurate evaluation of the effective mechanical properties of composites mainly depends on the characteristics of representative volume elements (RVEs). This paper mainly investigates the RVE size. Additionally, the effect of volume fraction of reinforcement, the edge effect, and RVE types on the critical size are discussed. First, the Al/Ni multilayered composites were processed by nine cycles of the cross-accumulative roll bonding (CARB) method. Then, one type of RVEs was created based on cross-sectional micrographs of composites to consider their inhomogeneities. Another type was generated by using the random sequential adsorption (RSA) procedure. Thereafter, the homogenized effective elastic properties of both types of microstructure-based RVEs and RSA-based RVEs were computed and compared as a function of the volume fraction of Ni and RVE size. The results showed that by increasing the Ni fragments, the RVEs indicated stiffer elastic behavior. By increasing the volume fraction of Ni from 0.2 Vf to 0.8 Vf, the Poisson ratio decreased by 7 % and the elastic modulus increased by 83 % for RSA-based RVE. Regarding the size of microstructure-based RVE of Al/Ni (0.8 Vf), from the largest size (size 1) with a length of 575 μm and a width of 575 μm to the smallest size (size 5) with a length of 287.5 μm and a width of 287.5 μm, the elastic modulus and the Poisson ratio showed 16 % and 0.8 % decrease, respectively.

1. Introduction

Over the past decades, the engineered materials have developed in industries. Some of these materials include composites, metamaterials, metallic glasses, polymers, and alloys [1–5]. Nickel and its alloys are good examples of these materials due to their interesting features [6–8]. Owing to providing a variety of outstanding properties, materials can be designed to satisfy the requirements of various applications [9–13]. The behavior of accordion metallic dampers has been studied by Nateghi [14]. Abolghasemi et al. [15] examined the strongback performance of a structure. Also, the mechanical properties of beams for space structures has been investigated by Emami and Gross [16]. Among these newly designed materials, composites are extensively manufactured [17–21]. For example, Qian et al. [19] have studied damage accumulation in C/SiC composites. Yuan et al. [22] examined the thermal properties of aluminum matrix composite. Emami and Kabir [23] have investigated the performance of composite under impact

* Corresponding author.
E-mail addresses: amir.h.assari1991@gmail.com, a_assari@sut.ac.ir (A.H. Assari).

https://doi.org/10.1016/j.heliyon.2024.e36489
Received 24 April 2024; Received in revised form 14 August 2024; Accepted 16 August 2024
Available online 16 August 2024

loading. In addition, the manufacturing techniques have seen a great progress [24,25]. Behseresht and Park [26] produced polymeric composite through additive manufacturing and Alinaghizadeh et al. [27] fabricated cutting tools by wire electrical discharge machining. Also, Assari and Eghbali [28] processed the metal matrix composite by hot pressing and hot rolling methods.

Nowadays, optimizing the materials' properties and reducing the cost of experiments have urged researchers to employ simulation, modeling, and numerical calculations [29–33]. Mozafarjazi and Rabiee [34] have conducted a numerical study on ductility and energy absorption of RC shear walls. Additionally, Abbasi-Ghiri et al. [35] studied the finite element models of the spine. Nasiri and Wang [36] employed kinematic simulation for precision force-controlled tasks in manufacturing. Moreover, Bazmi et al. [37] investigated the density functional theory (DFT) calculations for Cr-based composite. Hashemi et al. [38] carried out a finite element model of the wind turbine blade. In addition, the prediction of performance and properties of materials and components is increasingly becoming popular in industries. The deformation behavior of the hot-pressed composite was estimated by Assari [39]. The neural network-based prediction of energy consumption has been performed by Momeni et al. [40]. Additionally, Shabani and Kaviani-Hamedani have predicted the permanent vertical and shear strains over cyclic loading of the subsoil layer [41]. Also, predicting the performance of the thermal storage unit was done by Kiaghadi et al. [42]. Moreover, Patadia and Sweat [43] have investigated the importance of integrating the actual micro-nanostructures from imaging and multiscale models for realistic simulations of hybrid composites.

Effective properties of composite generally depend on its substances and microstructural configurations including size, aspect ratio, and volume fraction of reinforcement. To estimate these properties, several micromechanical theories namely the Shear-lag model, Mori-Tanaka model method, and finite element approach have been developed. More complicated representative volume elements (RVEs) have been successfully modeled through the finite element approach [44]. By using this approach, up to now, a wide range of composites such as fiber-reinforced polymer composites and ceramic-reinforced metal composites have been studied. Nonetheless, in metal laminated composite, there is still limited research on different aspects of finite element analysis and representative volume element modeling which may include element type, mesh size, boundary conditions, types of loading, RVE types, and RVE size.

Generally, the types of RVEs are divided into microstructure-based RVE and simplified RVE. The former considers inhomogeneities of actual microstructure based on the micrograph's images taken from cross-sections of samples [8,39]. However, the latter is based on the distribution of simple shapes in a specific area [45]. Up to now, several procedures have been introduced to create the RVE with the random distribution of the second phase within a matrix. The random sequential adsorption (RSA) has recently received much attention [46]. This technique sequentially adds the reinforcement to the defined domain and simultaneously checks their over-lapping. Yuanwu et al. [8] have recently created the two-dimensional RVEs of aluminum matrix composites by RSA method. Also, to validate the computed results by RVE modeling, different mechanical experiments should be carried out. Among them, tensile testing is extensively used. For example, Elbana et al. [47] have done tensile test to evaluate the reliability of FEA analyses of composite. Kumar Sahu and Sreekanth [48,49] performed tensile tests for SiC-reinforced polyethylene composite and HDPE based polymer matrix nanocomposite reinforced with nanodiamond for validating the FEM based representative volume element approach.

The determination of critical RVE size to analyze effective properties at a macroscopic scale is of great importance. On the one hand, it needs to be large enough to possess the right content of substances alongside their correct geometries which usually appear as inhomogeneities and irregularities, particularly sharp corners. On the other hand, it should be small enough to reduce the computation cost and time. For example, Kanit et al. [50] reported different RVE sizes for effective elastic and thermal properties. In addition, Savvas et al. [51] reported different convergency rates of results concerning RVE size in determining the properties. These studies clearly show the importance of critical RVE size. Moreover, there are numerous investigations about the evaluation of RVE size in polymeric and ceramic composites. With regard to metallic composites, the RVE size was only examined by Assari [39] in Ti/Al/Ti multilayered composites. He processed this composite by using the hot-pressing method and then the microstructure-based RVEs in which the layers were all continuous were created. Two sizes of three-dimensional RVEs were studied with the dimensions of $3.23 \times 3.23 \times 3.23\ mm^3$ and $0.0008 \times 0.0008 \times 0.0008\ mm^3$. It was pointed out that the larger size could better predict the elastic properties. This was mainly because of two reasons including correct stacking of layers and volume fractions of composites' substances. The larger RVE was created as $Ti/TiAl_3/Al/TiAl_3/Ti$ while the smaller was in the form of $Ti/TiAl_3/Al$. However, there is still a shortcoming of investigations about RVE size, especially when the reinforcing layer is not continuous and is distributed within the matrix.

One of the determining factors in capturing effective properties by finite element analysis (FEA) is the type of boundary conditions. The impact of boundary conditions on simulated results has been widely investigated in recent years. One of the most recent studies which was done by Yuanwu et al. [8] reported the effectiveness of periodic boundary conditions for evaluating the elastic properties of Al/Ni multilayered composites. It is widely acknowledged that applying this boundary condition is a time-consuming procedure and often results in high-frequency oscillations [52]. Also, matching nodes on the periodic boundary faces may not be possible, especially in the presence of irregularities. For example, in severely deformed metal composites where the periodic distribution of the second phase within the matrix never exists, imposing this boundary condition is extremely challenging. In previous investigation, the periodic boundary condition was only exerted on RSA-generated RVEs. Thus, when there are a large number of RVEs with different sizes and substances' contents, the periodic boundary condition can be replaced with other boundary conditions. Among them, symmetric boundary condition has always been of interest in recent investigations due to its ease of application [53].

This study, for the first time, evaluates the RVE size in metal-metal composites. To this end, the aluminum/nickel multilayered composites were processed by nine CARB cycles. The microstructure-based RVEs and RSA-based RVEs were modeled, based on the microstructure of composites from SEM imaging. In each RVE type, the edge effect and different volume fractions of nickel were considered in determining various RVE sizes and their related elastic properties. Furthermore, the reliability of predicted values was assessed by the experimental tensile properties.

2. Materials and methods

2.1. Starting materials and pre-annealing treatment

The elemental sheets of Ni (99.5 wt % Ni; 0.1 wt % Si; 0.1 wt % Fe; 0.1 wt % Cu; 0.05 wt % Mn) and Al (99.5 wt % Al; 0.05 wt % Si; 0.09 wt % Fe; 0.005 wt % Cu; 0.001 wt % Mn), were used in the current study. The starting sheets, as mentioned in Ref. [8], were used with a length of 200 mm and a width of 200 mm, and different thicknesses were chosen for four different sandwiches and volume fractions. The values of thickness are listed in Table 1. As shown, the same thickness of Al was used for Al/Ni composites while only the thickness of Ni varies to obtain specific volume fractions.

The initial sheets of Al (at 400 °C for 150 min) and Ni (at 600 °C for 150 min) were annealed to reduce their internal stress and increase their deformation capability.

2.2. Surface preparation and stacking of sheets

After pre-annealing treatment, the sheets were surface-prepared by cleaning in acetone and wire-brushing. Once the surface preparation was done, the sheets were stacked together in the order of Al/Ni/Al, as illustrated in Fig. 1a.

2.3. Procedure of CARB process

The composite processing has been previously stated in the literature [22]. However, the procedure is summarized below:

The roll bonding of Al/Ni (0.2 Vf), Al/Ni (0.4 Vf), Al/Ni (0.6 Vf), and Al/Ni (0.8 Vf) sandwiches were carried out under thickness reductions of 53 %, 58 %, 66 %, and 77 %, as shown in Fig. 1b. This is related to their different initial thicknesses. Thus, after the first cycle of the CARB process, all four processed sandwiches had equal thickness. Then, they were cut in two halves, surface-prepared, and stacked together, as depicted in Fig. 1c. The second CARB cycle was performed by a 90-degree rotation of rolling direction (RD) around normal direction (ND) and then roll bonding under 50 % thickness reduction, as shown in Fig. 1d. This cycle was repeated seven more times. Finally, Al/Ni (0.2 Vf), Al/Ni (0.4 Vf), Al/Ni (0.6 Vf), and Al/Ni (0.8 Vf) composites fabricated by nine CARB cycles were achieved.

2.4. Microstructural analysis

To investigate the microstructure of Al/Ni (0.2 Vf), Al/Ni (0.4 Vf), Al/Ni (0.6 Vf), and Al/Ni (0.8 Vf) composites, different characterization instruments including scanning electron microscopy (SEM) with backscattered electron detector, energy dispersive spectroscopy (EDS), and X-ray diffractometry (XRD) were used.

2.5. Tensile test

To conduct the tensile test, the samples from each composite were machined, as shown in Fig. 2. Then, the tests were done as detailed in the literature [8].

3. RVE modeling

To model the deformation behavior of composites, two types of RVEs were created and the edge-effects were also considered in RSA-based RVEs as described in detail in the previously published paper [8]. All fragments of nickel were assumed to be aligned towards the rolling direction in each RVE. The brief description of RVE models, edge-effect, and element type is as follows.

3.1. Microstructure-based RVEs

To include the irregularities of microstructure such as positions, different sizes and shapes of broken layers, the microstructure-based RVEs were created based on the SEM images of microstructures. The backscattered electron (BSE) images were segmented by using Image J analysis software and then converted to digital micrographs in Abaqus CAE software, as illustrated in Fig. 3(a–d).

Table 1
Initial thickness of Al and Ni sheets (in ***mm***).

	Initial thickness of Al sheet	Initial thickness of Ni sheet
Al/Ni (0.2 Vf)	**0.5**	**0.08**
Al/Ni (0.4 Vf)	**0.5**	**0.2**
Al/Ni (0.6Vf)	**0.5**	**0.5**
Al/Ni (0.8 Vf)	**0.5**	**1.2**

* Vf: volume fraction.

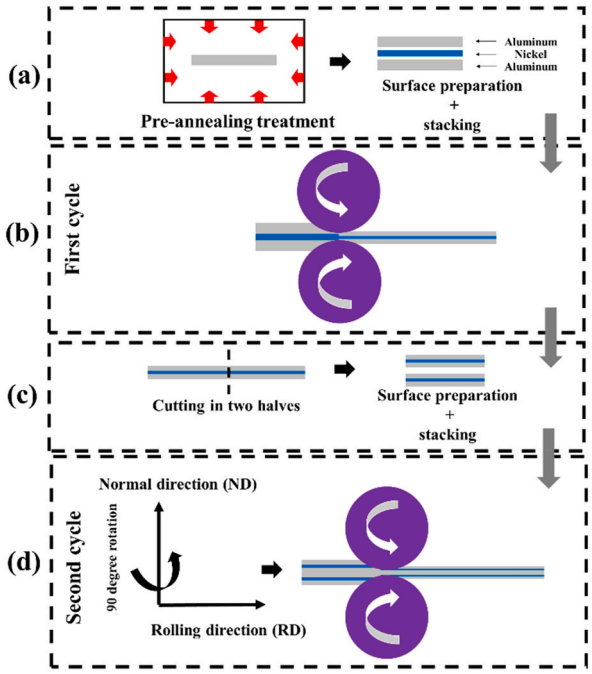

Fig. 1. The schematic showing different steps of the Al/Ni composites production including (a) pre-annealing/surface-preparing/stacking of layer sheets, (b) roll bonding, (c) cutting/surface-preparing/stacking of processed composites, and (d) 90° rotation of rolling direction/roll bonding.

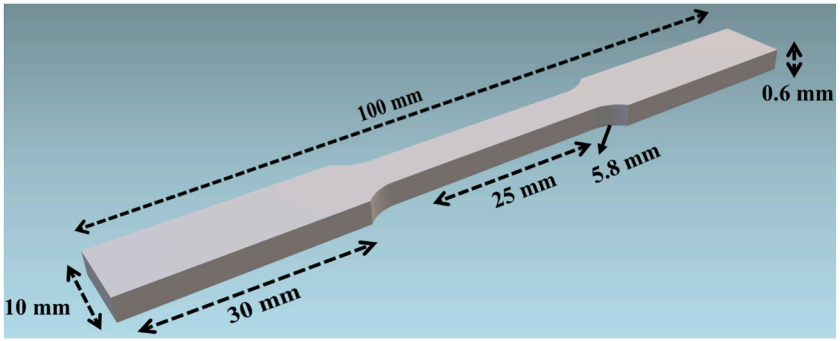

Fig. 2. The schematic of the standard tensile sample of Al/Ni composite.

3.2. RSA-based RVEs

Since in metal-metal composites processed by severe plastic deformation, the broken layers are randomly distributed in matrix, the random sequential adsorption (RSA) algorithm as a powerful method for creating RVEs was employed in this research. The 2D RVEs were generated by sequential addition of ellipses with different dimensions into the rectangular space. During this random distribution, to avoid the interactions of fragments, the overlapped ellipses were removed. Then, the procedure continued to reach the specified volume fractions of the second phase. Also, based on the minimum distance between the fragments of the actual microstructure, the distance between ellipses was defined. This also helped to avoid the occurrence of mesh problems between ellipses and the matrix. The generated RVEs are exhibited in Fig. 4a and b.

3.2.1. RVEs without edge-effects

In these RVEs, no ellipse can penetrate through the edge of the RVE, as shown in Fig. 4b.

3.2.2. RVEs with edge-effects

In these RVEs, the ellipses were allowed to penetrate through the edge of the RVE, as shown in Fig. 4a. However, each penetrated ellipse appeared on the opposite edge of RVE. To maintain the periodicity of distributed ellipses, all ellipses which cross the edges were cut and shifted to the opposite edges.

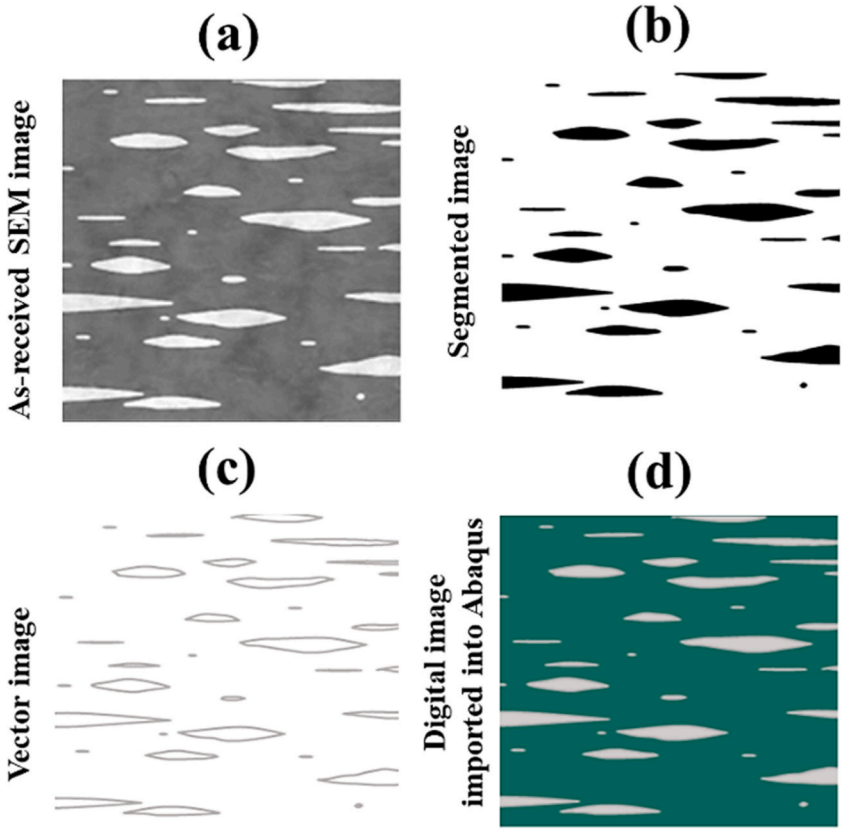

Fig. 3. Steps of designing the microstructure-based RVE, (a) SEM image, (b) segmented image, (c) vector image, and (d) digital image imported into Abaqus.

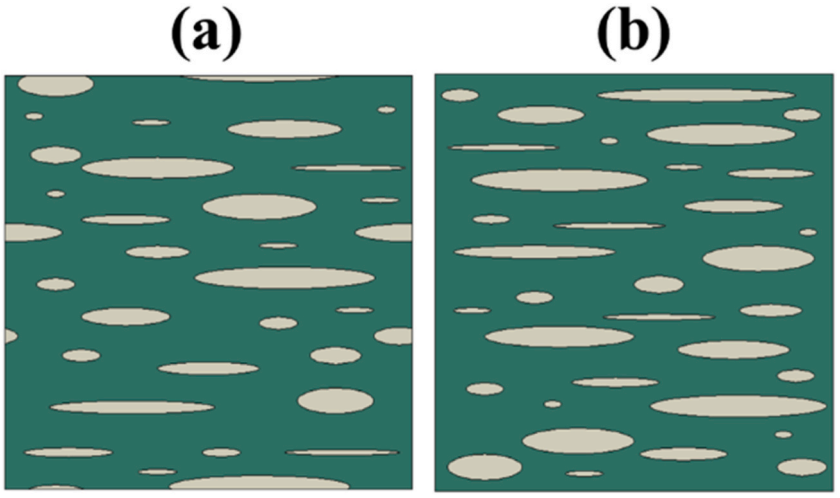

Fig. 4. The outcome of created RVEs by RSA method: (a) with edge effect and (b) without edge effect.

A perfect bonding at the interface of the Al matrix and Ni fragments was considered in all RVEs. Considering the elastic-plastic behavior of Al and Ni, the material properties (Table 2) used in the model were assigned to the matrix and reinforcement. Also, the following equations (equations (1) and (2)) were employed for linear elastic and elastoplastic constitutive responses of composites.

$$\sigma = E \,.\, \varepsilon \text{ - when } \sigma < \sigma_Y \tag{1}$$

Table 2
The input parameters of composites' constituents for multi-scale simulation.

	Elastic modulus, GPa	Shear modulus, GPa	Yield strength, MPa	Poisson's ratio
Al	75	26	190	0.35
Ni	200	79	285	0.31

$$\sigma = \sigma_Y . \left(\frac{\varepsilon}{\varepsilon_Y}\right)^n \text{ - when } \sigma \geq \sigma Y \tag{2}$$

in these equations, σ, ε, σ_Y, ε_Y, E, and n are uniaxial stress, uniaxial strain, yield strength, yield strain, elastic modulus, and strain-hardening exponent, respectively. Also, due to the irregular shape of Ni fragments, the linear triangular elements of type CPS3 were adopted. The different number of elements were used to analyze the mesh convergence for each RVE. The number of elements changed for different RVEs depending on volume fraction and RVE size. Additionally, different RVE sizes were compared to accurately investigate the numerical-solution convergence.

3.3. Symmetric Boundary Condition (SBC)

As depicted in Fig. 5, the displacements of the nodes on the left and bottom edges were restricted in the Y and X directions, respectively. this means that the nodes on the left edge can move in the X direction while the nodes on the bottom edges can only move in the Y direction. The other two edges can move freely in the X and Y directions.

All analyses were conducted by applying a strain of 0.7 % along the X-axis.

The volume average of stress and strain in the tensile direction were calculated based on the homogenization method [54], as given in equations (3) and (4).

$$\overline{\sigma_i} = \frac{1}{V}\int_V \sigma_i dV \tag{3}$$

$$\overline{\varepsilon_i} = \frac{1}{V}\int_V \varepsilon_i dV \tag{4}$$

where i denotes the direction of the stress/strain tensor.

To obtain the average values of elastic modulus and Poisson ratio, equations (5) and (6) were used.

$$\nu = \frac{-\varepsilon_y}{\varepsilon_x} \tag{5}$$

$$E = (1+\nu)(1-2\nu)\frac{\sigma_X}{\varepsilon_X + \varepsilon_Y} \tag{6}$$

The extracted values were plotted as a function of volume fraction and RVE size.

4. Results and discussion

4.1. Morphology of composites

The SEM micrographs of Al/Ni (0.2 Vf) and Al/Ni (0.8 Vf) composites versus CARB cycles are illustrated in Fig. 6(a–h). The

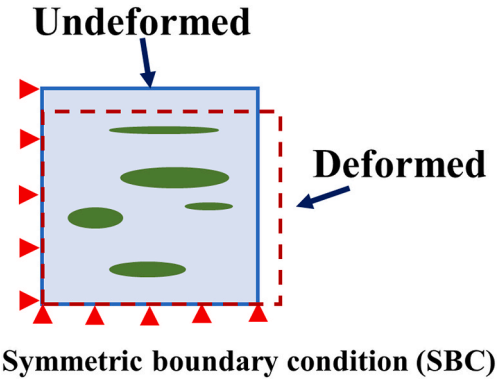

Fig. 5. The illustration showing the initial and final status of the RVE with symmetric boundary condition subjected to tensile loading.

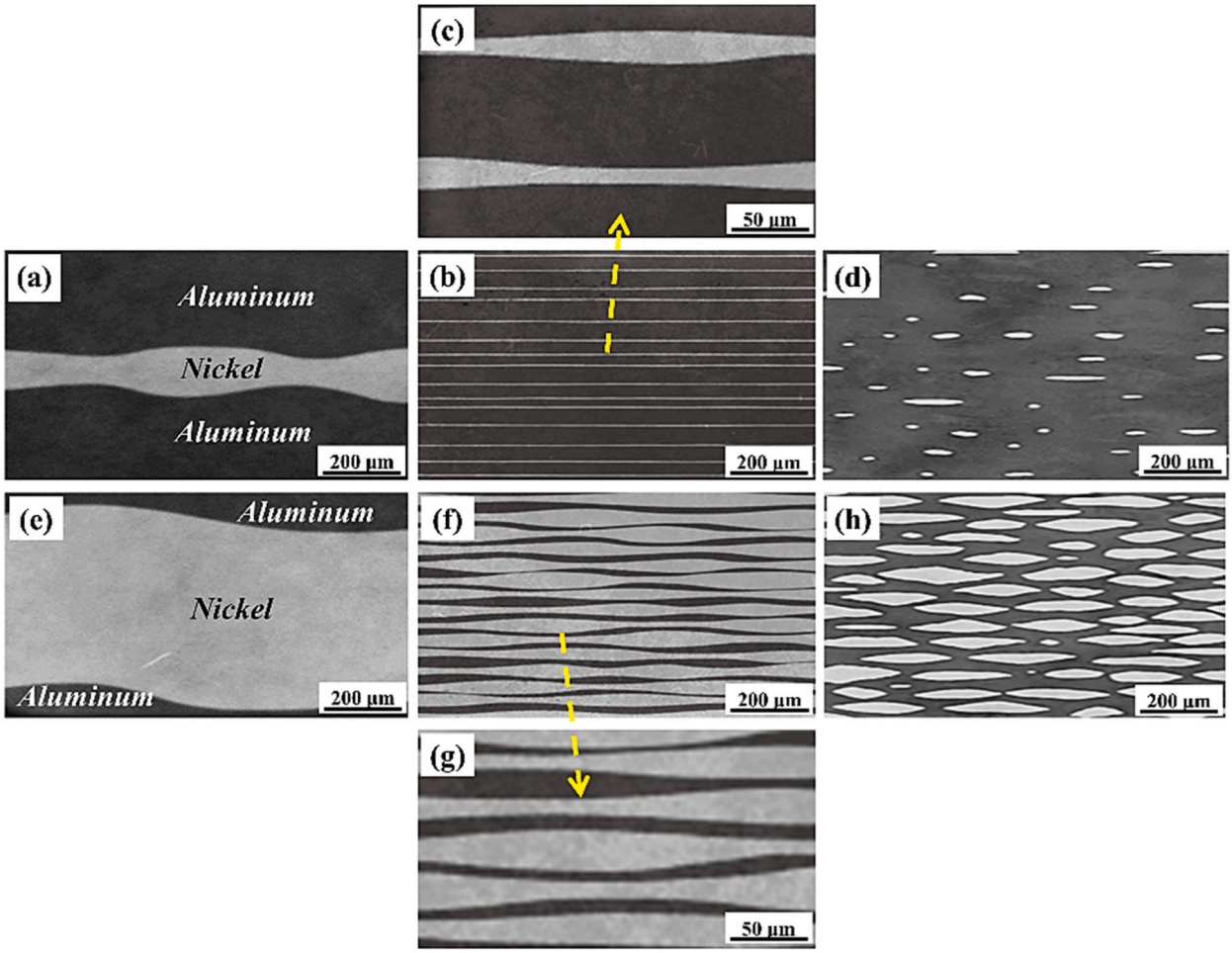

Fig. 6. SEM images of Al/Ni (0.2Vf) and Al/Ni (0.8Vf) composites at: (a and e) first cycle, (b, c, f, and g) fifth cycle, and (d and h) ninth CARB cycles. And (c and g) magnified images of the fifth cycle.

microstructures of both composites with the thinnest and thickest Ni layers show clear changes by increasing cycles. These changes include reduction of layers' thickness, waviness of interfaces, necking of harder layers, layers rupture, and distribution of broken layers. These are typical features of severely deformed composites and are extensively reported in the literature [8,55,56]. As reported by Su et al. [57], the applied plastic strain cause thickness reduction. The waviness of interfaces, as shown in Fig. 6 (a, b, c, e, f, g) stems from the nonuniform distribution of shear deformation [58]. Then, Yang et al. pointed out that [59] the localized strain promotes necking of Ni layers. The necked layers finally experience rupture, as shown in Fig. 6d and h. These phenomena heterogeneously occur in different regions, leading to the distribution of broken layers of Ni. However, as reported by Zou et al. [56], both pre-annealing of starting layers and changing strain path result in better deformability of layers under the rolling process. This declines strain localization which then maintains layers' continuity to higher cycles. These positive impacts altogether promote a more uniform distribution of Ni layers within the Al matrix. However, the main reason of such irregular changes is attributed to different strain rate sensitivity of

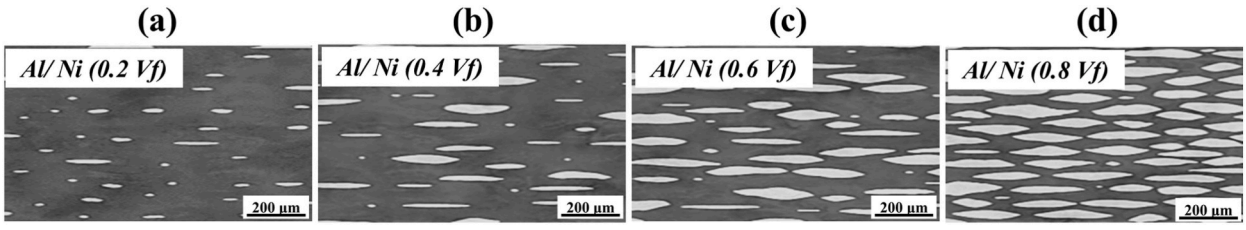

Fig. 7. Micrographs of Al/Ni composites as a function of volume fraction of Ni: (a) 0.2 Vf, (b) 0.4 Vf, (c) 0.6 Vf, and (d) 0.8 Vf after ninth CARB cycles.

composites' substances which varies from one metal to another. For example, different co-deformation in Al/Ni and Al/Mg composites leads to significantly different microstructures [22,56]. This is related to the limited deformability of Mg alloys with HCP structure compared to Ni with FCC structure [8,56].

It is commonly believed that the plastic strains induced by roll bonding are not equally distributed across the composites' thickness. In fact, the largest strain located on the surfaces of the sandwich decreases to its center. This is attributed to the friction between samples and rollers when there is no lubrication [60,61].

The geometrically necessary dislocations are generated as a result of strain incompatibility between layers with different flow properties [62]. Also, the formation of shear bands around bonded surfaces of Al and Ni can be responsible for the rupture of Ni layers. According to the literature, higher cycles of rolling need to be carried out to reach the homogenized distribution of Ni fragments.

In contrast to the published papers [63,64], as can be seen in Fig. 7(a–d), the homogeneous distribution of Ni fragments was achieved through the pre-annealing of initial sheets and applying the CARB process. However, this homogeneity requires severe plastic deformation or higher CARB cycles because the formation of shear bands can affect the orientation and distribution of fragments [64].

Fig. 8a and b shows the XRD patterns on raw metal sheets and Fig. 8c and d shows XRD analyses performed on rolling direction (RD)-normal direction (ND) regions of Al/Ni (0.2Vf) and Al/Ni (0.6Vf) composites. These characterizations revealed a variety of crystallographic planes including (111), (200), (311), and (220) for Al and Ni. This diversity in crystallographic planes is the main feature of FCC metals, confirming their high deformability. To more accurately examine the existence of the interphases, the EDS analysis was carried out at the interfaces of Al/Ni, as shown in Fig. 9a and b. The result in Fig. 9c did not reveal any intermetallic compounds. It is deduced that applying cold roll bonding did not result in the formation of unexpected intermetallic compounds at the bonded interfaces.

4.2. tensile test

The results of the tensile test are illustrated in Fig. 10. The stress-strain curves are shown in Fig. 10a and the extracted results are shown in Fig. 10b. The correlation between CARB cycles and tensile properties of Al and Ni sheets is evident. The ultimate strength increases whereas the elongation shows a reduction. Such behavior is usually observed when metal layers are subjected to severe plastic deformation. It is widely acknowledged that strain hardening of layers during initial cycles and grain refinement during the final cycles are responsible for the occurrence of such tensile behavior [65]. The first effect, based on the Taylor hardening relationship

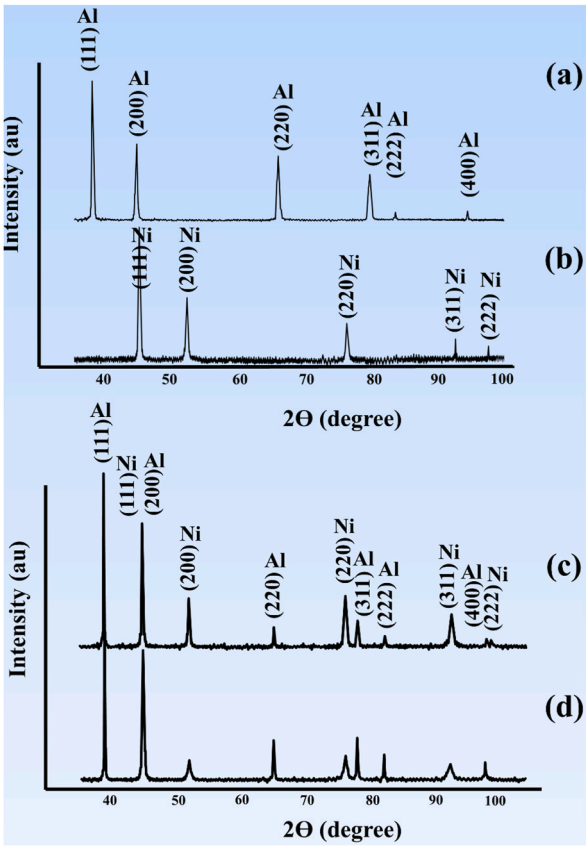

Fig. 8. X-ray diffraction patterns of: (a) raw Al sheet, (b) raw Ni sheet, and Al/Ni composites with (c) 0.6 Vf, and (d) 0.2 Vf of Ni.

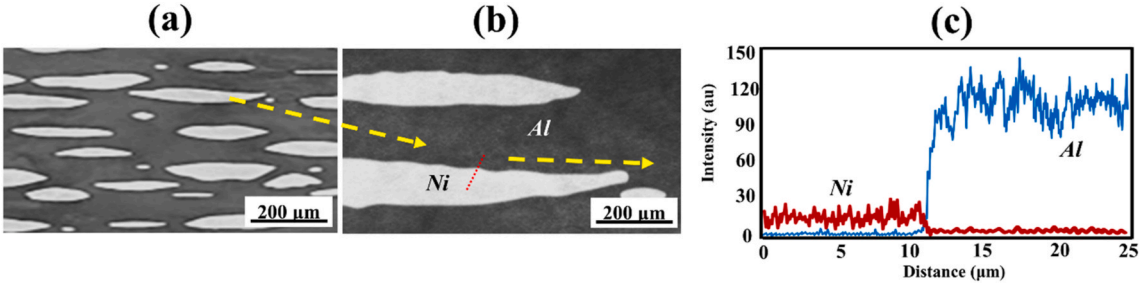

Fig. 9. (a and b) BSE images at different magnifications (c) EDS line analysis at the Al/Ni interface.

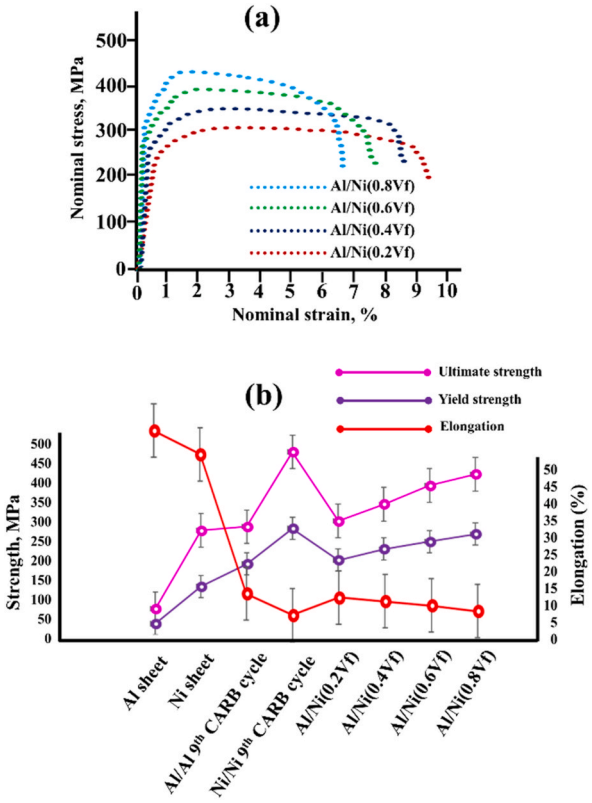

Fig. 10. (a) engineering stress-strain curves of composites with different volume fractions of Ni [8] and (b) yield strength, ultimate strength, and elongation for Al and Ni sheets and Al/Ni composites.

[66], improves the strengths by increasing the density of dislocation and their pile-up while the second effect, based on the Hall-Petch relationship [67], increases strengths by increasing the number of grain boundaries. The change of strain path during the CARB process is believed to be a cause of strength enhancement. This method as reported by Yang et al. [68] can significantly enhance the deformability of metals even the HCP metals with limited slip systems. This enhancement was reported in the recently published paper [56] in the fabrication of Al/Mg composites by pre-annealing of layers and the CARB process.

From Fig. 10, the effect of volume fraction on stress-strain curves can be seen. When subjected to tension, the dislocation movement occurring on slip systems usually controls the deformation of the composite. During the strain-hardening of layers, the intersection and pile-up of dislocations occur. This is the main reason for the increase in strength and reduction of elongation concerning the laminated composites during the CARB process. However, an increase in the number and size of Ni fragments from Al/Ni (0.2 Vf) and Al/Ni (0.8 Vf) is another affecting factor on dislocation movement. Indeed, the Orowan loops are probably created by the fragments. To leave these loops behind and have further movement, the dislocations need more tensile stress. This is consistent with the literature wherein the homogeneously distributed reinforcement within the matrix has a positive impact on mechanical properties [69,70].

Zou et al. [56] pointed out that the higher tensile strength and elongation of CARBed-composites compared to ARBed-composite stems from the uniformity in its microstructure. As mentioned in the previous section, uniformity occurs since layers are elongated in

all directions on the TD-RD plane during successive cycles. Comparing the results of the current study with those reported in the literature [65,71] further strengthens the effect of pre-annealing and the CARB process in enhancing the tensile properties of composites.

4.3. Finite element analysis

The effect of the volume fraction of Ni, RVE size, and edge effect on the elastic behavior of created RVEs are studied. As previously mentioned, the 2D RVEs have been recently modeled in the recent investigation [8]; however, all RVEs, here, are under symmetric boundary condition (SBC) to efficiently evaluate the critical RVE size.

4.3.1. Influence of volume fractions

Fig. 11(a–d) shows the distribution of Von Mises stress in microstructure-based RVEs with changing volume fractions. The maximum values appear adjacent to the fragments, particularly their sharp corner. Similarly, these regions were subjected to strain localization, as demonstrated in Fig. 12. The strain localization of RVEs concerning Al/Ni (0.4 Vf) and Al/Ni (0.6 Vf) are shown in Fig. 12a and b. Furthermore, the stress concentration and strain localization rose versus the content of the second phase. Similar findings were reported in the recent investigation [8] in which two other boundary conditions including periodic boundary condition (PBC) and kinematic boundary condition (KBC) were employed on RVEs of Al/Ni composite. It is believed that stress concentration and strain localization take place where there are irregularities and materials with different flow behaviors [8,39]. Furthermore, as reported by Liu et al. [72] who simulated the hot-pressed aluminum/steel composites, the difference between the deformation of aluminum and steel layers during compression resulted in shear stress appearing as stress concentration.

It is generally believed that the harder phase endures the increasing stress during deformation. The localized strain is seen near these phases because it is believed that the harder phases induce strain accumulation in the soft phase [73]. Yu et al. [74] who generated RVE with different aspect ratios of Ti fragments for rolled Ti/Al composites reported that when the aspect ratio increases, higher concentrated stress concentration and localized strain appeared. In fact, by increasing the aspect ratio of fragments, the distance between them declines and more stress and strain are accumulated in the matrix between fragments.

Comparing Figs. 11 and 13 shows a little discrepancy between the values of Mises stress. In Al/Ni (0.2 Vf) and Al/Ni (0.4 Vf), slightly higher stress is concentrated in microstructure-based RVEs. This is attributed to the irregular shapes and sharper corners of fragments. Gao et al. [75] reported the stress concentration at the corner of SiC particles in Al matrix. Nonetheless, at a higher volume fraction, the Von Mises values of RSA-based RVEs, as shown in Fig. 13(a–d), show larger values than the other RVEs. This is probably related to the differences in their volume fractions. In the actual microstructure of multilayered composites processed by severe plastic deformation, the distribution of the second phase is not completely uniform while, in RSA-generated RVEs, the periodicity of the randomly distributed fragments could reach the exact volume fractions. Thus, a higher content of the second phase (Ni) increases the Von Mises stress. In addition, Ghayoor et al. [76] pointed out the uneven distribution of stress near irregular shapes in composites.

The homogenized values of the elastic constants versus volume fraction of the second phase achieved by finite element analysis of RVEs were plotted in Fig. 14a and b. Evidently, all elastic values are significantly affected by the content of Ni. However, the main reason why the calculated values of modulus are larger than the experimentally achieved ones is that the composite becomes stricter when SBC is exerted. It has been reported by Qing [77] that the elastic constants of Ti–Al_3Ti core-shell structured particulate reinforced

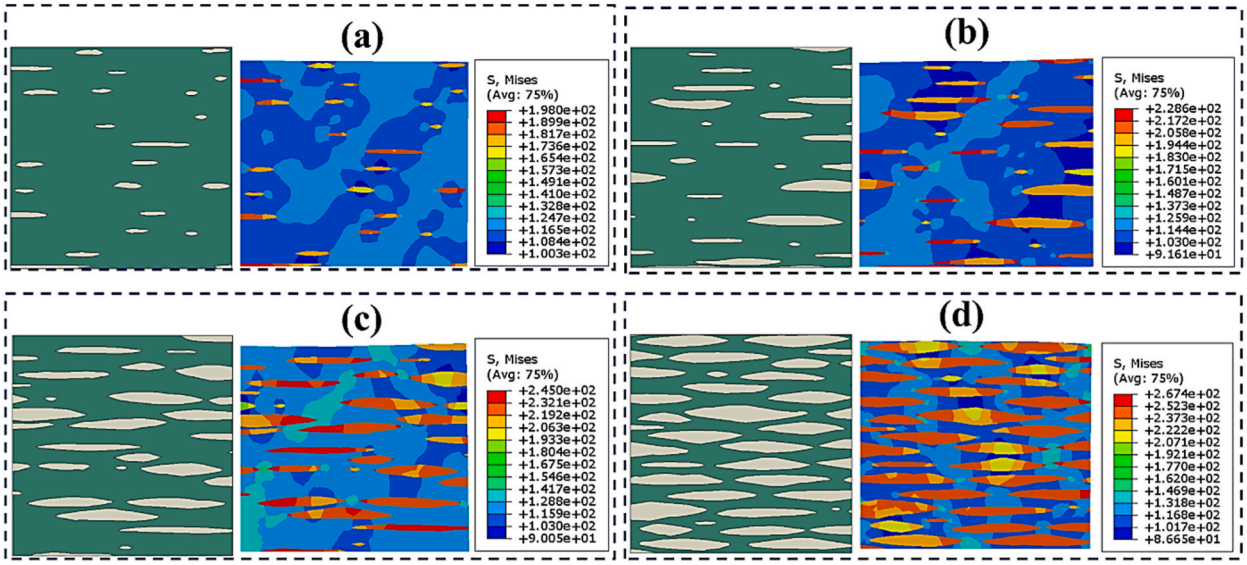

Fig. 11. Contour plots of Von Mises stress of microstructure-based RVEs versus volume fraction of Ni: (a) 0.2 Vf, (b) 0.4 Vf, (c) 0.6 Vf, and (d) 0.8 Vf.

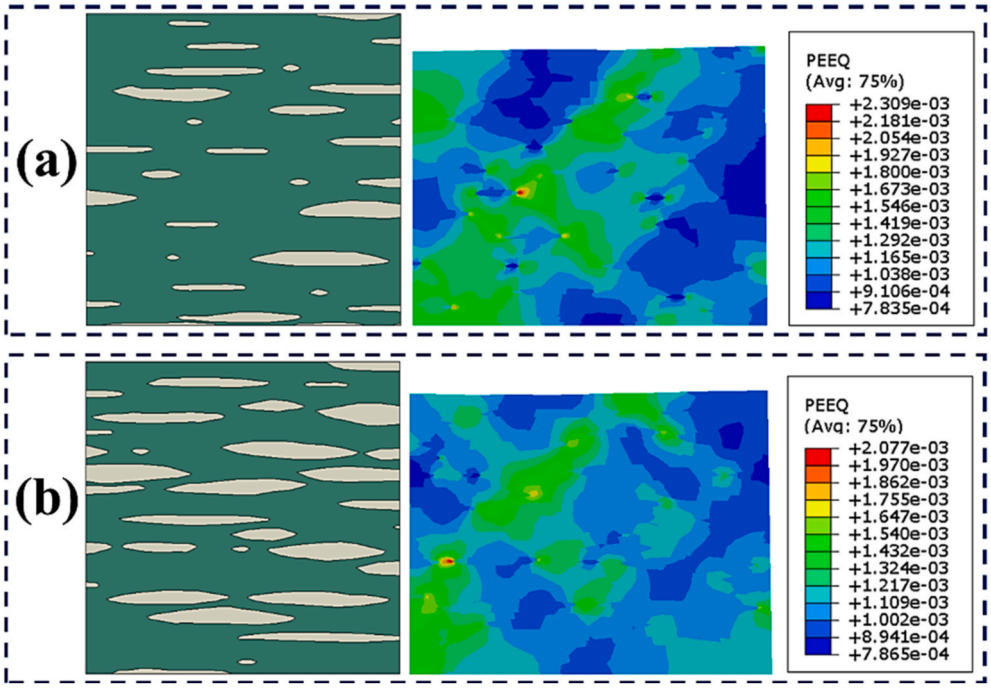

Fig. 12. Contour plots of the equivalent plastic strain of microstructure-based RVEs: (a) Al/Ni (0.4 Vf) and (b) Al/Ni (0.6 Vf).

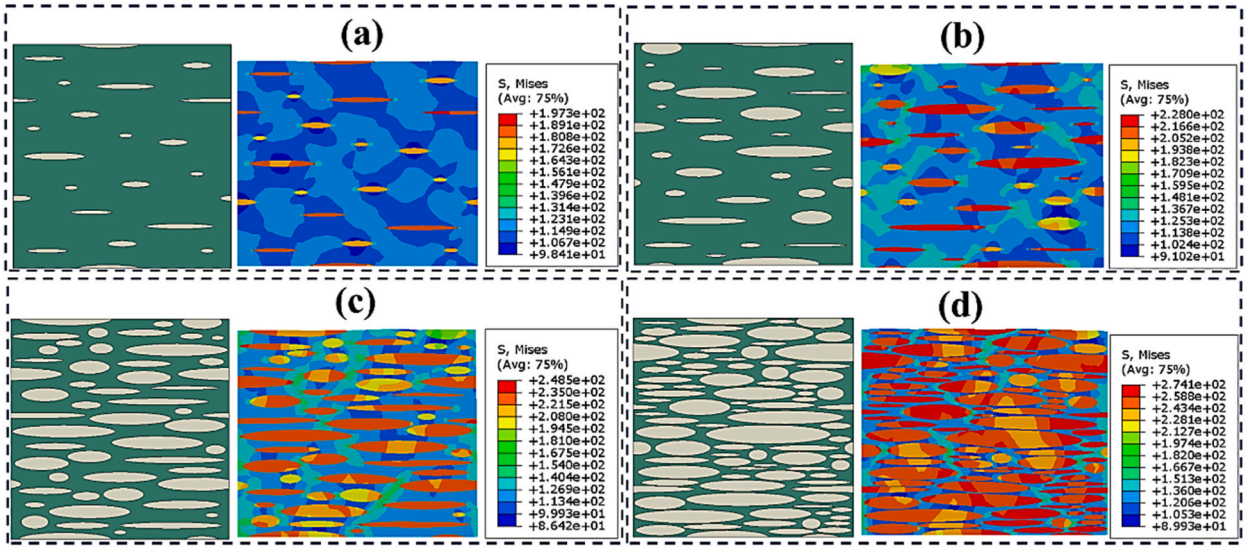

Fig. 13. Contour plots of Von Mises stress of RSA-based RVEs with edge effect versus the volume fraction of Ni: (a) 0.2 Vf, (b) 0.4 Vf, (c) 0.6 Vf, and (d) 0.8 Vf.

A356 composite under SBC and PBC were different. The former results in higher values than those achieved by experiments while the latter brings about lower values than experiments. As reported by Denisiewicz et al. [78], the linear boundary condition compared to the uniform traction boundary conditions results in a stiffer response due to its more restricted condition.

Comparing the elastic moduli and Poisson's ratio of both RVEs in Fig. 15a and b shows little scatter. In fact, in lower volume fractions, the results are relatively equal while at higher volume fractions, the RSA-based RVEs seem stiffer. Such behavior can be observed in the flow behavior of RVEs in Fig. 15.

4.3.2. The effect of edge

The periodic distribution of the second phase in RVE models of composites is vital when the periodic boundary condition is applied.

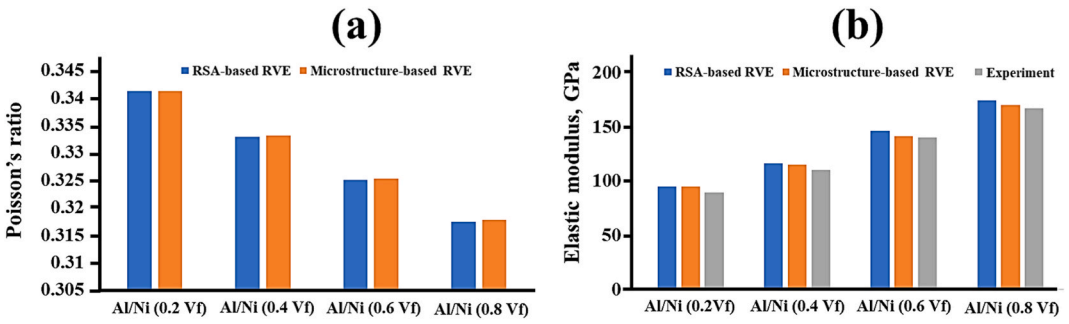

Fig. 14. Predicted (a) Poisson's ratio and (b) elastic modulus of both types of RVEs versus different volume fractions of Ni.

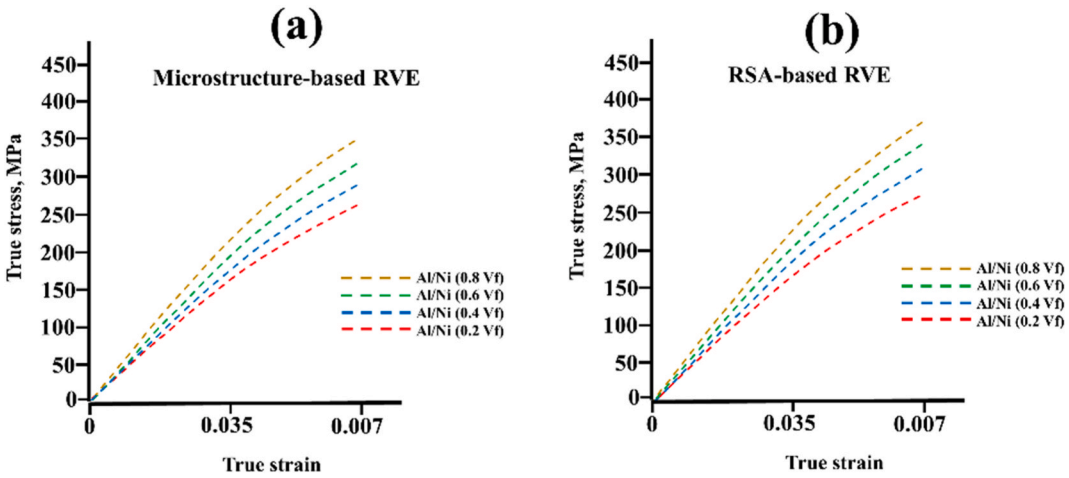

Fig. 15. Stress-strain relationships of different micromechanical models: (a) microstructure-based RVEs and (b) RSA-based RVEs versus volume fraction of Ni.

Also, this represents an ideal distribution of phases in each representative volume element. Furthermore, Li et al. [79] have reported that considering the edge effect enables acquiring RVE models with a high volume fraction of the second phase. To consider the impact of edge effect on elastic properties, two RVEs were created by RSA method. In one RVE, all fragments were randomly distributed without crossing the edges of the matrix. The other RVE, on the other hand, consists of randomly distributed fragments with probable crossing the matrix edges. More importantly, to achieve the periodicity of fragments, those fragments that cross the edges should reappear on the opposite edge, as illustrated in Fig. 13. The Von Mises distribution of RVEs with no edge effect is exhibited in Fig. 16 (a–d). Comparing Figs. 13 and 16 indicates that the RVEs with no edge effect are more rigid. In addition, higher stress is concentrated on the fragments. Also, Cui et al. [73] conducted an investigation on microstructure-based modeling of the compressive deformation behavior of an aluminum alloy in which a network of Al–Cu phases existed. They showed that low and high levels of local stress were concentrated near the soft aluminum phase and hard interphases, respectively. This shows that the hard phases with higher strengths are responsible for bearing the stress. Additionally, Farid et al. [80] reported higher stress concentrations near larger TiC particles.

From Fig. 17a and b, the stiffer elastic behavior of the RVEs with no edge effect is evident. Their elastic moduli are higher while they possess a lower Poisson's ratio than the RVEs with edge effect. It is concluded that the predicted elastic values of RVEs with edge effect give better prediction than the RVEs without edge effect.

4.3.3. Influence of RVE size

To evaluate the critical RVE size, five sizes of microstructure-based RVEs and RSA-based RVEs were created. The RVE sizes decreased from a maximum size of 575 μm^2 (size 1) to a minimum size of 287.5 μm^2 (size 5). Regarding the microstructure-based RVEs, the previously considered RVEs (Figs. 18 and 19) which have the largest width were partitioned into smaller sizes. By doing this, the effect of fragment irregularities and distribution were also taken into account. It should be noted that the RVE sizes are different while the images with equalized dimensions have been shown in Figs. 18 and 19. Obviously, there is the same distribution of stress across the RVEs. It has been reported that sharp morphologies are prone to high-stress concentration. High stress near interfaces often appears since the hard phases restrict the local deformation of the soft phase [73].

Nevertheless, their homogenized elastic properties change as a function of RVE size. However, the influence of RVE size on Poisson's ratio is relatively smaller for Al/Ni (0.2 Vf) and Al/Ni (0.4 Vf) composites. On the contrary, the variation of elastic modulus

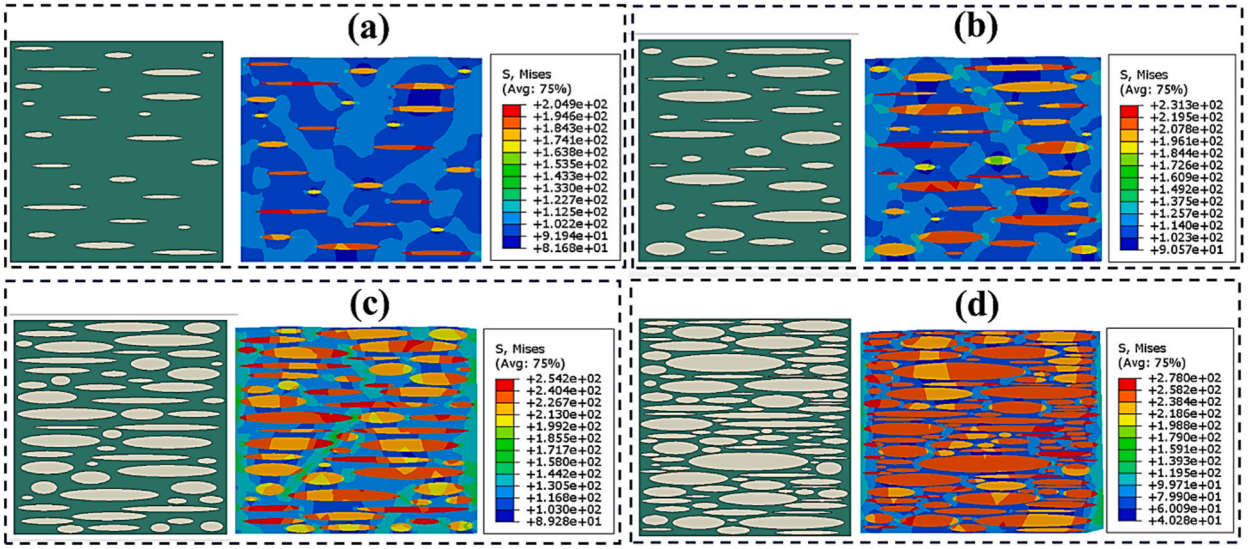

Fig. 16. Contour plots of Von Mises stress of RSA-based RVEs without edge effect versus volume fraction of Ni: (a) 0.2 Vf, (b) 0.4 Vf, (c) 0.6 Vf, and (d) 0.8 Vf.

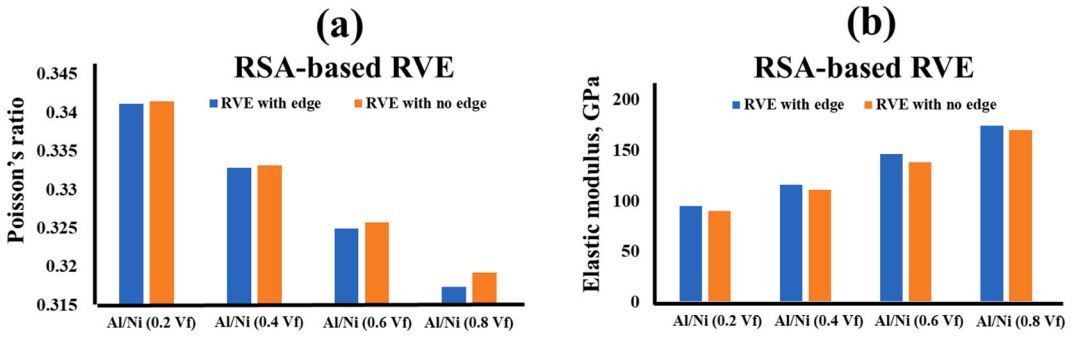

Fig. 17. Predicted (a) Poisson's ratio and (b) elastic modulus of RSA-based RVEs with and without edge effect. versus volume fraction of Ni.

was noticeable. The steeper reduction in values was observed for all RVEs except the one with Vf = 0.4 Ni which shows the rise of values. This may be attributed to the large fragments of Ni. In fact, the aspect ratio of fragments in the smallest RVE (size 5) is comparable to the largest RVE (size 1). This finding matches well with the previously published paper [39] in which the small RVE with the thick intermetallic layer showed stiffer behavior. However, from Fig. 20a and b, it can be seen that the results of Poisson ratio and elastic modulus converge with the increase of the RVE size. As reported by Trias et al. [81], in polymeric composites the aspect of fiber and element are determining factors for obtaining the critical RVE size. However, in metal composites, volume fraction, irregularities, and distribution of the second phase should be taken into account.

Different sizes of RSA-based RVEs are illustrated in Fig. 21a and b. For Al/Ni (0.2 Vf) and Al/Ni (0.4 Vf) as illustrated in Fig. 21, the Ni volume fraction was fixed to be 0.2 and 0.4. To obtain the suitable size of the RVE, the effective elastic properties of different sizes of RVEs were determined. The variation of effective properties of composites in response to the change in the size of RVE is shown in Fig. 22a and b. For all given volume fractions, the RVE size evidently affects the elastic modulus and Poisson's ratio. Also, a similar downward trend was observed for all predicted elastic constants with a decrease in RVE sizes. By enlarging the RVE size, the elastic modulus and Poisson's ratio improved slightly up to reaching convergence values. These findings are in agreement with the recent investigation of the RVE size of Ti/Al/Ti composites [39]. It has been reported that the RVE represents more reliable results when their size is as large as the actual thickness of the composite. This is mainly because the largest RVE size consists of more irregularities and, more importantly, in microstructure-based RVE, can satisfy the right volume fraction of the second phase.

The simulated stress-strain curves concerning different sizes of RVEs are plotted in Fig. 23a and b. The stress-strain curves of RVE show no significant discrepancies regardless of RVE size. By increasing the RVE size, the elastic region becomes sharper and converges with the large ones. However, the evident differences can be seen in RVEs of the Al/Ni (0.4 Vf) composite. With an increase in RVE size, the flow behavior first declined, then, increased slightly up to the largest RVE.

From the findings of predicted elastic behavior, it is deduced that enlarging the RVE size leads to the convergence of the computed results. Also, the largest RVEs (size 1) which were as thick as the actual composites give a better estimation of mechanical properties in

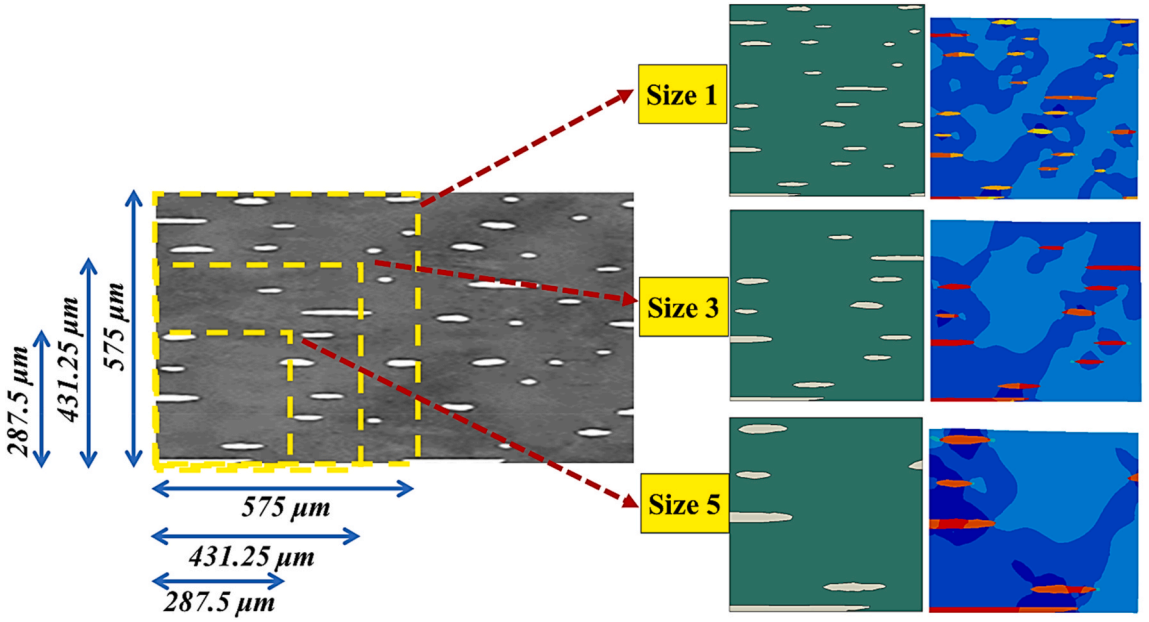

Fig. 18. Different RVE sizes and their Von Mises stress distribution of microstructure-based RVEs of Al/Ni (0.2 Vf).

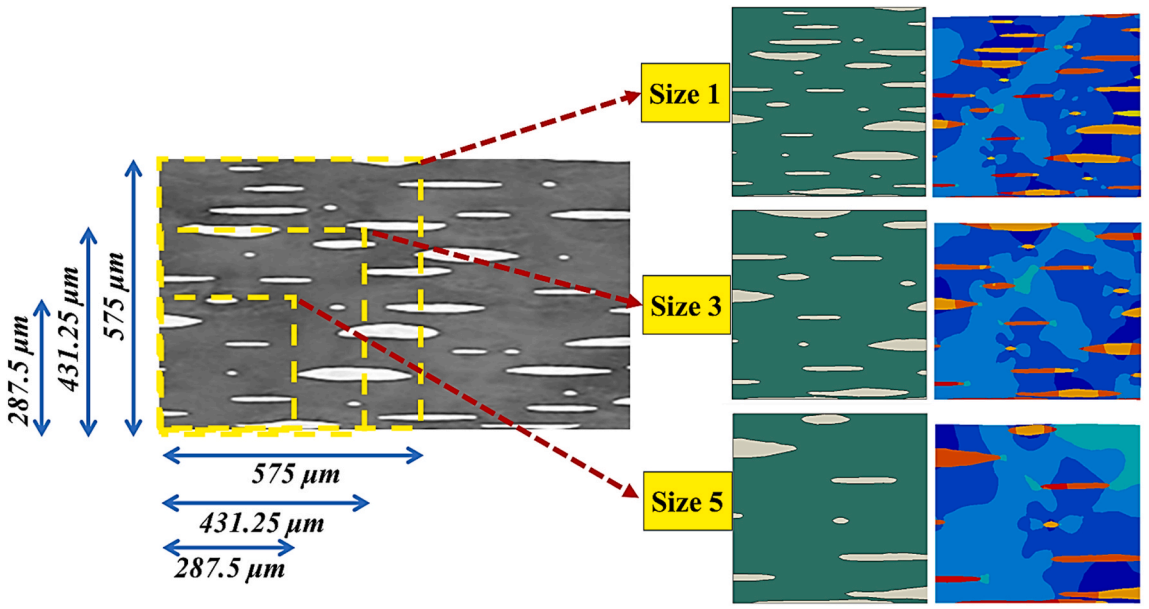

Fig. 19. Different RVE sizes and their Von Mises stress distribution of microstructure-based RVEs of Al/Ni (0.4 Vf).

2D simulation. This critical RVE size matches well with the estimated results in 3D simulation [39].

5. Conclusion

The aim of this research was to investigate the RVE size for the evaluation of the effective elastic properties of Al/Ni composite with different volume fractions of Ni by using finite element simulation of 2D RVE models and homogenization scheme. Two types of RVEs were created. The microstructure-based RVEs were modeled by using the micrographs images taken from the composites while the RSA-based RVEs were generated based on simplified geometries and by employing the RSA method. The edge effect which represents the periodicity of the distributed phase in the matrix was also considered in RSA-based RVEs.

The main findings are summarized below.

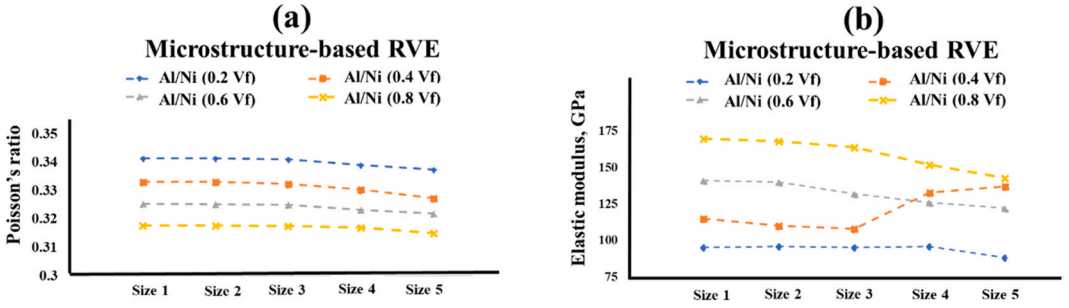

Fig. 20. Variation of predicted (a) Poisson's ratio and (b) Elastic modulus of microstructure-based RVEs with different sizes versus volume fraction of Ni.

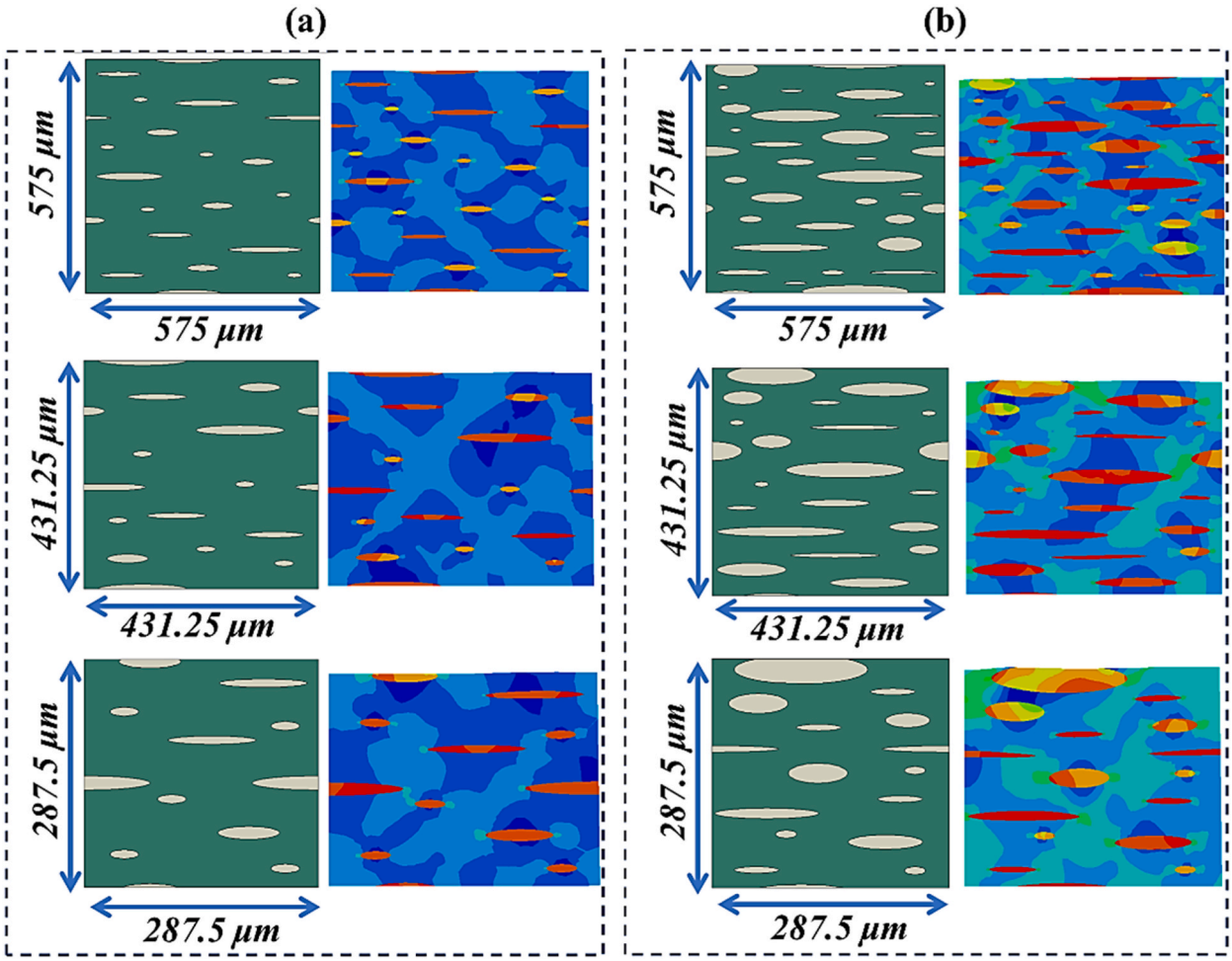

Fig. 21. Different RVE sizes and their Von Mises stress distribution of RSA-based RVEs: (a) Al/Ni (0.2 Vf) and (b) Al/Ni (0.4 Vf).

1. From the details of microstructural characterization, it is highlighted that the modification of microstructure was achieved through the pre-annealing and cross-accumulative roll bonding of sandwiches. Therefore, the ellipsoidal fragments of Ni were relatively uniformly distributed within the matrix. In addition to the strong bonding of interfaces without any evident void, according to EDS and XRD analyses, no unexpected intermetallic compounds were detected in composites, particularly at Al/Ni interfaces.
2. With an increase in Ni content, the results of tensile tests showed an improvement in elastic modulus, yield, and ultimate strengths. Accordingly, the values of elongation experienced a downward trend.

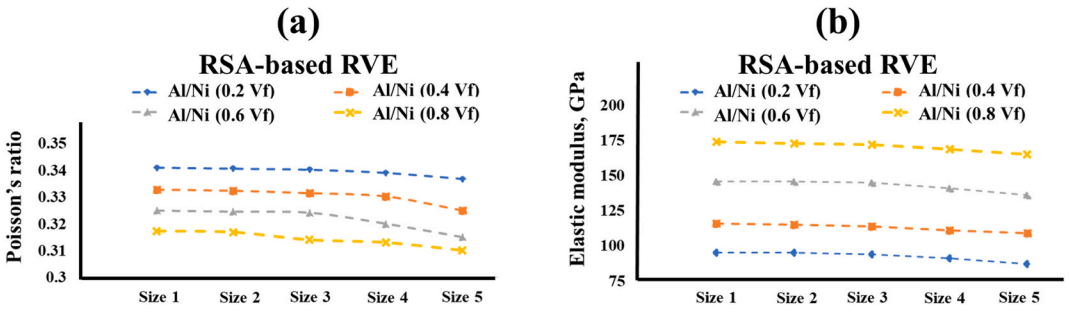

Fig. 22. Variation of predicted (a) Poisson's ratio and (b) Elastic modulus of RSA-based RVEs with different sizes versus volume fraction of Ni.

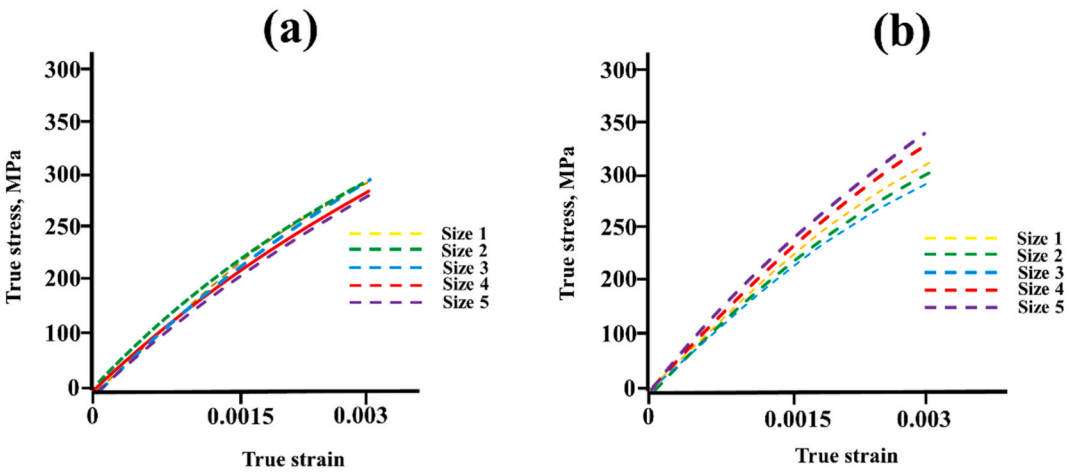

Fig. 23. Stress-strain relationships of different sizes of: (a) microstructure-based RVEs and (b) RSA-based RVEs Al/Ni (0.4 Vf) composite.

3. Both microstructure-based and RSA-based RVEs were capable of achieving satisfactory effective properties under symmetric boundary conditions. The only discrepancy between the experimental and the computed results is related to the stiffer behavior of composite under SBC. The calculated elastic properties indicate that finite element simulation of both types of RVEs gives a satisfactory prediction.
4. Five RVE sizes from the largest RVE with a length of 575 μm and a width of 575 μm to the smallest one with length of 287.5 μm and width of 287.5 μm were created. The computed elastic constants and the obtained stress-strain curves revealed the convergence of results by increasing the RVE size. The largest RVE size showed the elastic modulus of 170 GPa and the lowest Poisson ratio of 0.3177 for microstructure-based RVEs while elastic modulus of 174 GPa and the lowest Poisson ratio of 0.3173 were obtained for RSA-based RVE. Indeed, the large RVEs could estimate the elastic constants of the Al/Ni composites with higher accuracy.
5. The RSA-based RVEs with edge effect exhibited stiffer elastic behavior compared to RSA-based RVEs without edge effect which presented an elastic modulus of 170 GPa and the lowest Poisson ratio of 0.3192.

Data availability

The raw/processed data required to reproduce these findings cannot be fully shared at this time due to technical or time limitations.

CRediT authorship contribution statement

Amir Hossein Assari: Writing – original draft, Visualization, Validation, Methodology, Investigation, Formal analysis, Conceptualization. **Negar Shaghaghi:** Writing – review & editing, Visualization, Validation, Software, Investigation, Data curation. **Saeid Yaghoobi:** Writing – review & editing, Validation, Resources, Methodology, Funding acquisition, Formal analysis. **Sahar Ghaderi:** Writing – original draft, Visualization, Methodology, Investigation, Formal analysis, Data curation.

Declaration of competing interest

The authors declare that they have no known competing financial interests or personal relationships that could have appeared to influence the work reported in this paper.

References

[1] H. Ding, P. Gong, W. Chen, Z. Peng, H. Bu, M. Zhang, X. Tang, J. Jin, L. Deng, G. Xie, Achieving strength-ductility synergy in metallic glasses via electric current-enhanced structural fluctuations, Int. J. Plast. 169 (2023) 103711.
[2] J. Song, Y. Chen, X. Hao, M. Wang, Y. Ma, J. Xie, Microstructure and mechanical properties of novel Ni–Cr–Co-based superalloy GTAW joints, J. Mater. Res. Technol. 29 (2024) 2758–2767.
[3] J. Xiang, J. Chen, Y. Zheng, P. Li, J. Huang, Z. Chen, Topological design for isotropic metamaterials using anisotropic material microstructures, Eng. Anal. Bound. Elem. 162 (2024) 28–44.
[4] P. Monfaredi, S.M.M. Emami, A.S. Moghadam, Seismic behavior of hollow-core infilled steel frames; an experimental and numerical study, J. Constr. Steel Res. 192 (2022) 107244.
[5] S. Oshaghi, Nano-sized magnetic molecularly imprinted polymer solid-phase microextraction for highly selective recognition and enrichment of sulfamethoxazole from spiked water samples, J. Chromatogr. A (2024) 465016.
[6] Q. Gong, M. Cai, Y. Gong, M. Chen, T. Zhu, Q. Liu, Grinding surface and subsurface stress load of nickel-based single crystal superalloy DD5, Precis. Eng. 88 (2024) 354–366.
[7] B. Xie, H. Li, Y. Ning, M. Fu, Discontinuous dynamic recrystallization and nucleation mechanisms associated with 2-, 3-and 4-grain junctions of polycrystalline nickel-based superalloys, Mater. Des. 231 (2023) 112041.
[8] S. Yuanwu, A.H. Assari, S. Yaghoobi, M. Mahmoodi, S. Ghaderi, D. Ran, Influence of volume fractions and boundary conditions on the predicted effective properties of Al/Ni composites for industrial design, Metall. Mater. Trans. 55 (1) (2024) 118–133.
[9] D. Tang, G. Xiang, J. Guo, J. Cai, T. Yang, J. Wang, Y. Han, On the optimal design of staved water-lubricated bearings driven by tribo-dynamic mechanism, Phys. Fluids 35 (9) (2023).
[10] D. Tang, K. Xiao, G. Xiang, J. Cai, M. Fillon, D. Wang, Z. Su, On the nonlinear time-varying mixed lubrication for coupled spiral microgroove water-lubricated bearings with mass conservation cavitation, Tribol. Int. (2024) 109381.
[11] M. Hemmati, T. Messadi, H. Gu, J. Seddelmeyer, M. Hemmati, Comparison of embodied carbon footprint of a mass timber building structure with a steel equivalent, Buildings 14 (5) (2024) 1276.
[12] P. Monfaredi, M. Nazarpour, A.S. Moghadam, Influence of hollow-core wall panels on the cyclic behavior of different types of steel framing systems, PCI J. 66 (5) (2021).
[13] M. Nazarpour, P. Monfaredi, A.S. Moghadam, Experimental evaluation of hollow-core wall orientation in steel moment frame, PCI J. 64 (2019) 92–103.
[14] F. Nateghi, Improved behaviour of accordion metallic dampers affected by the increasing number of layers, Int. J. Eng. 28 (6) (2015) 864–870.
[15] S. Abolghasemi, N.E. Wierschem, M.D. Denavit, Impact of strongback on structure with varying damper and stiffness irregularity arrangements, J. Constr. Steel Res. 213 (2024) 108333.
[16] F. Emami, A.J. Gross, Mechanical Properties of Hierarchical Beams for Large-Scale Space Structures, AIAA SCITECH 2023 Forum, 2023, p. 384.
[17] Y. Jiang, L. Liu, J. Yan, Z. Wu, Room-to-low temperature thermo-mechanical behavior and corresponding constitutive model of liquid oxygen compatible epoxy composites, Compos. Sci. Technol. 245 (2024) 110357.
[18] Y. Mu, Y. Jin, H. Ji, J. Luo, G. Li, M. Xu, H. Li, B. Deng, J. Du, Mechanical performance of interpenetrating phase composites with multi-sheet lattice structures, Int. J. Mech. Sci. 276 (2024) 109369.
[19] W. Qian, W. Zhang, S. Wu, Y. Hu, X. Zhang, Q. Hu, S. Dong, S. Tu, In situ X-ray imaging and numerical modeling of damage accumulation in C/SiC composites at temperatures up to 1200° C, J. Mater. Sci. Technol. 197 (2024) 65–77.
[20] Y. Zhao, J. Jing, L. Chen, F. Xu, H. Hou, Current research status of interface of ceramic-metal laminated composite material for armor protection, Acta Metall. Sin. 57 (9) (2021) 1107–1125.
[21] F.M. Boroujeni, G. Fioravanti, R. Kander, Synthesis and characterization of cellulose microfibril-reinforced polyvinyl alcohol biodegradable composites, Materials 17 (2) (2024) 526.
[22] J. Yuan, A.H. Assari, S. Ghaderi, S. Yaghoobi, Characterization of microstructure, texture, grain structure, and thermal properties of Al/Ni/Al multilayered composites fabricated through cross-accumulative roll bonding, Vacuum (2024) 113423.
[23] F. Emami, M.Z. Kabir, Performance of Composite Metal Deck Slabs under Impact Loading, Structures, Elsevier, 2019, pp. 476–489.
[24] Y. Chen, S. Sun, T. Zhang, X. Zhou, S. Li, Effects of post-weld heat treatment on the microstructure and mechanical properties of laser-welded NiTi/304SS joint with Ni filler, Mater. Sci. Eng., A 771 (2020) 138545.
[25] Y. Wu, B. Deng, X. Li, Q. Li, T. Ye, S. Xiang, M.-C. Zhao, A. Atrens, In-situ EBSD study on twinning activity caused by deep cryogenic treatment (DCT) for an as-cast AZ31 Mg alloy, J. Mater. Res. Technol. 30 (2024) 3840–3850.
[26] S. Behseresht, Y.H. Park, Additive manufacturing of composite polymers: thermomechanical FEA and experimental study, Materials 17 (8) (2024) 1912.
[27] A. Alinaghizadeh, M. Hadad, B. Azarhoushang, Experimental study of the surface quality of form-cutting tools manufactured via wire electrical discharge machining using different process parameters, Micromachines 14 (11) (2023) 1976.
[28] A.H. Assari, B. Eghbali, Solid state diffusion bonding characteristics at the interfaces of Ti and Al layers, J. Alloys Compd. 773 (2019) 50–58.
[29] M. Gan, X. Chong, T. Lu, C. Yang, W. Yu, S.-L. Shang, Y. Wang, Z.-K. Liu, J. Feng, Unveiling thermal stresses in RETaO4 (RE= Nd, Sm, Eu, Gd, Tb, Dy, Ho and Er) by first-principles calculations and finite element simulations, Acta Mater. 271 (2024) 119904.
[30] X. Long, K. Chong, Y. Su, C. Chang, L. Zhao, Meso-scale low-cycle fatigue damage of polycrystalline nickel-based alloy by crystal plasticity finite element method, Int. J. Fatig. 175 (2023) 107778.
[31] X. Long, K. Chong, Y. Su, L. Du, G. Zhang, Connecting the macroscopic and mesoscopic properties of sintered silver nanoparticles by crystal plasticity finite element method, Eng. Fract. Mech. 281 (2023) 109137.
[32] S.A. Abdollahi, A. Pourabadeh, M. Alishiri, A. Sodagartojgi, S.F. Ranjbar, M.B. Ehghaghi, F. Talati, Modeling and optimization of efficient removal of diclofenac and naproxen based on chemometric approaches, Water Resour. Ind. 31 (2024) 100238.
[33] F. Hamedi, O.R. Ranjbar-Naeini, A. Layeghi, A. Heidariazar, M.I. Zibaii, H. Latifi, Self-referred microcavity-based fused-fiber fabry-perot refractometer, Opt. Fiber Technol. 68 (2022) 102753.
[34] M. Mozafarjazi, R. Rabiee, Experimental and numerical study on the load-bearing capacity, ductility and energy absorption of RC shear walls with opening containing zeolite and silica fume, Engineering Solid Mechanics 12 (3) (2024) 237–246.
[35] A. Abbasi-Ghiri, M. Ebrahimkhani, N. Arjmand, Novel force–displacement control passive finite element models of the spine to simulate intact and pathological conditions; comparisons with traditional passive and detailed musculoskeletal models, J. Biomech. 141 (2022) 111173.
[36] E. Nasiri, L. Wang, Hybrid force motion control with estimated surface normal for manufacturing applications. arXiv Preprint arXiv:2404.04419, 2024.
[37] M. Bazmi, A. Rashidi, A. Naderifar, F. Tabarkhoon, M.S. Alivand, F. Tabarkhoon, M.V. Farahani, M.D. Esrafili, Simultaneous enhancement of CO2 adsorption capacity and kinetics on a novel micro-mesoporous MIL-101 (Cr)-based composite: experimental and DFT study, J. CO2 Util. 83 (2024) 102809.
[38] A. Hashemi, J. Jang, S. Hosseini-Hashemi, Semi-analytical analysis for dynamic behaviors of wind turbine blades using transfer function methods, topics in modal analysis & testing, volume 8. Proceedings of the 39th IMAC, A Conference and Exposition on Structural Dynamics 2021, Springer, 2022, pp. 33–43.
[39] A.H. Assari, Investigating the deformation behavior of hot-pressed Ti/Al/Ti laminated composite, J. Manuf. Process. 95 (2023) 369–381.
[40] S. Momeni, A. Eghbalian, M. Talebzadeh, A. Paksaz, S.K. Bakhtiarvand, S. Shahabi, Enhancing office building energy efficiency: neural network-based prediction of energy consumption, Journal of Building Pathology and Rehabilitation 9 (1) (2024) 1–14.
[41] F. Shabani, F. Kaviani-Hamedani, Cyclic response of sandy subsoil layer under traffic-induced principal stress rotations: application of bidirectional simple shear apparatus, Soil Dynam. Earthq. Eng. 164 (2023) 107573.
[42] M. Kiaghadi, M. Sheikholeslami, A. Alinia, F.M. Boora, Predicting the performance of a photovoltaic unit via machine learning methods in the existence of finned thermal storage unit, J. Energy Storage 90 (2024) 111766.

[43] M. Patadia, R. Sweat, Modelling and analysis of multiscale hybrid composite structures for virtual design and performance-driven manufacturing: a review. Advances in Materials and Processing Technologies, 2024, pp. 1–36.
[44] S. Bargmann, B. Klusemann, J. Markmann, J.E. Schnabel, K. Schneider, C. Soyarslan, J. Wilmers, Generation of 3D representative volume elements for heterogeneous materials: a review, Prog. Mater. Sci. 96 (2018) 322–384.
[45] F. Han, F. Roters, D. Raabe, Microstructure-based multiscale modeling of large strain plastic deformation by coupling a full-field crystal plasticity-spectral solver with an implicit finite element solver, Int. J. Plast. 125 (2020) 97–117.
[46] E. Chang, A. Ameli, A.R. Alian, L.H. Mark, K. Yu, S. Wang, C.B. Park, Percolation mechanism and effective conductivity of mechanically deformed 3-dimensional composite networks: computational modeling and experimental verification, Compos. B Eng. 207 (2021) 108552.
[47] A. Elbana, A. Khennane, P.J. Hazell, Multiscale modelling of particulate composites with spherical inclusions, Eng. Comput. (2024) 1–27.
[48] S.K. Sahu, P.R. Sreekanth, Evaluation of tensile properties of spherical shaped SiC inclusions inside recycled HDPE matrix using FEM based representative volume element approach, Heliyon 9 (3) (2023) e36489.
[49] S.K. Sahu, P. Rama Sreekanth, Multiscale RVE modeling for assessing effective elastic modulus of HDPE based polymer matrix nanocomposite reinforced with nanodiamond, Int. J. Interact. Des. Manuf. (2022) 1–10.
[50] T. Kanit, S. Forest, I. Galliet, V. Mounoury, D. Jeulin, Determination of the size of the representative volume element for random composites: statistical and numerical approach, Int. J. Solid Struct. 40 (13–14) (2003) 3647–3679.
[51] D. Savvas, G. Stefanou, M. Papadrakakis, Determination of RVE size for random composites with local volume fraction variation, Comput. Methods Appl. Mech. Eng. 305 (2016) 340–358.
[52] W. Tian, L. Qi, X. Chao, J. Liang, M. Fu, Periodic boundary condition and its numerical implementation algorithm for the evaluation of effective mechanical properties of the composites with complicated micro-structures, Compos. B Eng. 162 (2019) 1–10.
[53] M. Einolghozati, A. Assempour, Mechanical behavior of spheroidized steel sheets: effects of microstructural features, loading, and boundary condition modeling, J. Mater. Eng. Perform. 32 (14) (2023) 6350–6364.
[54] I.V. Singh, A. Shedbale, B. Mishra, Material property evaluation of particle reinforced composites using finite element approach, J. Compos. Mater. 50 (20) (2016) 2757–2771.
[55] R.-E. Dong, A.H. Assari, S. Yaghoobi, M. Mahmoodi, S. Ghaderi, Effect of volume fraction of Ti on microstructure evolution and thermal properties of Al/Ti laminated composites, Met. Mater. Int. (2023) 1–13.
[56] Y. Zou, S. Guo, S. Tang, A.H. Assari, M. Azimi, S. Ghaderi, M. Mahmoodi, Enhancing grain refinement and mechanical properties of AA1100/MgAZ31/AA1100 composites by using different roll bonding techniques, Mater. Today Commun. 38 (2024) 108000.
[57] H. Su, L. Hou, Q. Tian, Y. Wang, L. Zhuang, Understanding the bending behavior and through-thickness strain distribution during asymmetrical rolling of high-strength aluminium alloy plates, J. Mater. Res. Technol. 22 (2023) 1462–1475.
[58] N. Nie, L. Su, G. Deng, H. Li, H. Yu, A.K. Tieu, A review on plastic deformation induced surface/interface roughening of sheet metallic materials, J. Mater. Res. Technol. 15 (2021) 6574–6607.
[59] D. Yang, P. Cizek, P. Hodgson, Ultrafine equiaxed-grain Ti/Al composite produced by accumulative roll bonding, Scripta Mater. 62 (5) (2010) 321–324.
[60] T. Inoue, A. Yanagida, J. Yanagimoto, Finite element simulation of accumulative roll-bonding process, Mater. Lett. 106 (2013) 37–40.
[61] D.C.C. Magalhães, O.M. Cintho, J.B. Rubert, V.L. Sordi, A.M. Kliauga, The role of shear strain during Accumulative Roll-Bonding of multilayered composite sheets: pattern formation, microstructure and texture evolution, Mater. Sci. Eng., A 796 (2020) 140055.
[62] I. Kapoor, Y. Lan, A. Rijkenberg, Z. Li, V. Janik, Quasi in-situ analysis of geometrically necessary dislocation density in α-fibre and γ-fibre during static recrystallization in cold-rolled low-carbon Ti-V bearing microalloyed steel, Mater. Char. 145 (2018) 686–696.
[63] C. Ji, Y. He, C.T. Wang, Y. He, X. Pan, J. Jiao, L. Guo, Investigation on shock-induced reaction characteristics of an Al/Ni composite processed via accumulative roll-bonding, Mater. Des. 116 (2017) 591–598.
[64] G. Min, J.-M. Lee, S.-B. Kang, H.-W. Kim, Evolution of microstructure for multilayered Al/Ni composites by accumulative roll bonding process, Mater. Lett. 60 (27) (2006) 3255–3259.
[65] X. Guo, Y. Ma, K. Jin, H. Wang, J. Tao, M. Fan, Effect of stand-off distance on the microstructure and mechanical properties of Ni/Al/Ni laminates prepared by explosive bonding, J. Mater. Eng. Perform. 26 (2017) 4235–4244.
[66] T. Ajantiwalay, X. Ma, A. Yu, M. Pole, J. Silverstein, S. Mathaudhu, A. Devaraj, B. Gwalani, Shear deformation of pure-Cu and Cu/Nb nano-laminates using micromechanical testing, Scripta Mater. 230 (2023) 115403.
[67] A. Saufan, S. Yu, J.-Y. Wang, Enhancement of mechanical properties for Mg-9Li-1Zn alloy by accumulative roll bonding, Mater. Res. Express 7 (4) (2020) 046511.
[68] Q. Yang, B. Jiang, B. Song, Z. Yu, D. He, Y. Chai, J. Zhang, F. Pan, The effects of orientation control via tension-compression on microstructural evolution and mechanical behavior of AZ31 Mg alloy sheet, J. Magnesium Alloys 10 (2) (2022) 411–422.
[69] M. Huang, C. Xu, G. Fan, E. Maawad, W. Gan, L. Geng, F. Lin, G. Tang, H. Wu, Y. Du, Role of layered structure in ductility improvement of layered Ti-Al metal composite, Acta Mater. 153 (2018) 235–249.
[70] A. Misra, X. Zhang, D. Hammon, R. Hoagland, Work hardening in rolled nanolayered metallic composites, Acta Mater. 53 (1) (2005) 221–226.
[71] K. Brunelli, L. Peruzzo, M. Dabalà, The effect of prolonged heat treatments on the microstructural evolution of Al/Ni intermetallic compounds in multi layered composites, Mater. Chem. Phys. 149 (2015) 350–358.
[72] B. Liu, H. Wang, G. Yan, H. Lin, Q. Jiang, Effect of reduction rate on microstructure and properties of laminated steel/aluminium low density composites prepared by hot pressing, Mater. Technol. 39 (1) (2024) 2329856.
[73] L. Cui, Z. Zhang, X.-G. Chen, Spatial reconstruction, microstructure-based modeling of compressive deformation behavior, and prediction of mechanical properties in lightweight Al-based entropy alloys, Mater. Des. 242 (2024) 113025.
[74] C. Yu, Y. Wu, Z. Yang, X. Shu, H. Xiao, Effect of Ti fracture on mechanical properties of accumulative-roll-bonded Ti–Al composite plates, J. Mater. Res. Technol. 25 (2023) 6702–6709.
[75] X. Gao, X. Zhang, M. Qian, A. Li, G. Wang, L. Geng, H.-X. Peng, Enhanced stress concentration sensitivity of SiCp/Al composite with network architecture, J. Compos. Mater. 56 (8) (2022) 1165–1174.
[76] H. Ghayoor, S.V. Hoa, C.C. Marsden, A micromechanical study of stress concentrations in composites, Compos. B Eng. 132 (2018) 115–124.
[77] H. Qing, Automatic generation of 2D micromechanical finite element model of silicon–carbide/aluminum metal matrix composites: effects of the boundary conditions, Mater. Des. 44 (2013) 446–453.
[78] A. Denisiewicz, M. Kuczma, K. Kula, T. Socha, Influence of boundary conditions on numerical homogenization of high performance concrete, Materials 14 (4) (2021) 1009.
[79] G. Li, F. Sharifpour, A. Bahmani, J. Montesano, A new approach to rapidly generate random periodic representative volume elements for microstructural assessment of high volume fraction composites, Mater. Des. 150 (2018) 124–138.
[80] W. Farid, H. Li, Z. Wang, H. Cui, C. Kong, H. Yu, Integrating experimental and computational analyses for mechanical characterization of titanium carbide/aluminum metal matrix composites, Materials 17 (9) (2024) 2093.
[81] D. Trias, J. Costa, A. Turon, J. Hurtado, Determination of the critical size of a statistical representative volume element (SRVE) for carbon reinforced polymers, Acta Mater. 54 (13) (2006) 3471–3484.